Electrochemical Performance of YST Infiltrated and Fe Doped YST Infiltrated YSZ Anodes for IT-SOFC

Sivaprakash Sengodan,[a] Jong Seol Yoon,[b] Mi Young Yoon,[b] Hae Jin Hwang,[b,*]
Jeeyoung Shin,[c] and Guntae Kim[a,z]

[a]*Interdisciplinary School of Green Energy, Ulsan National Institute of Science and Technology (UNIST), Ulsan 689-798, Korea*
[b]*School of Materials Science and Engineering, Inha University, Incheon 402-751, Korea*
[c]*Department of Mechanical Engineering, Dong-Eui University, Busan 614-714, Korea*

Donor doped and donor-acceptor co-doped strontium titanate perovskite are investigated for intermediate temperature solid oxide fuel cells (IT-SOFCs) anodes. $Y_{0.08}Sr_{0.88}TiO_{3-\delta}$ and $Y_{0.08}Sr_{0.92}Ti_{1-x}Fe_xO_{3-\delta}$ ($x = 0.2, 0.4$) anodes were prepared by infiltration in 65% porous yttria stabilized zirconia (YSZ) scaffolds. The microstructure and electrical conductivity of $Y_{0.08}Sr_{0.88}TiO_{3-\delta}$ and $Y_{0.08}Sr_{0.92}Ti_{1-x}Fe_xO_{3-\delta}$ strongly depends on Fe content. The conductivity of $Y_{0.08}Sr_{0.88}TiO_{3-\delta}$ and $Y_{0.08}Sr_{0.92}Ti_{1-x}Fe_xO_{3-\delta}$; decreases with increasing Fe content in humidified H_2. $Y_{0.08}Sr_{0.88}TiO_{3-\delta}$, $Y_{0.08}Sr_{0.92}Ti_{0.8}Fe_{0.2}O_{3-\delta}$, and $Y_{0.08}Sr_{0.92}Ti_{0.6}Fe_{0.4}O_{3-\delta}$, anodes with a Pd/CeO_2 catalyst show peak power density of 298, 421, and 321 mW cm^{-2}, respectively, in wet H_2 at 1073 K.
© 2013 The Electrochemical Society. [DOI: 10.1149/2.004306eel] All rights reserved.

In the last two decades solid oxide fuel cells (SOFCs) have shown great progress in terms of research and development activities. Beginning with the first working example of a SOFC demonstrated by Baur and Preis in 1937,[1] many new materials and designs have been realized.[2–7] The higher operating temperature of SOFC leads, however, to corrosion of SOFC components, high cost, and sealing difficulties. These problems have spurred the development of intermediate temperature solid oxide fuel cells (IT-SOFCs) that operate at 923 K to 1023 K. The electrode and electrolyte material used in IT-SOFC should be chemically, thermally, and mechanically stable at a wide range of $p(O_2)$ under SOFC operating conditions.

SOFCs have much greater fuel flexibility due to the characteristic that O^{2-} anions are the species transported through the membrane to the anode forming carbon dioxide, for example, when using hydrocarbon as a fuel. However, Ni-YSZ anodes show carbon deposition when exposed to hydrocarbons, leading to cell failure.[8] There is accordingly strong demand for the development of new materials capable of converting hydrocarbons while at the same time being tolerant to impurities.

The importance of identifying alternative anode materials for IT-SOFCs working on hydrocarbons has been recognized in the field of IT-SOFC research.[9] A and/or B site doped perovskite metal oxides ($AA'BB'O_3$) show stable performance as redox stable anodes both in H_2 and hydrocarbon fuels.[10,11] Among these metal oxides, donor doped $SrTiO_3$ has garnered considerable interest as anodes for IT-SOFCs. The conductivity, however, displayed by $SrTiO_3$ is too low for anode application. For anode application, the conductivity of $SrTiO_3$ can be increased either by partial substitution of Sr^{2+} by trivalent ions such as La^{3+}, Y^{3+}, and Gd^{3+} or by partial substitution of Ti^{4+} by pentavalent ions such as Nb^{5+}.[12] In the presence of trivalent ions in the A site and/or the reduction procedure, it is easier for Ti^{4+} to reduce to Ti^{3+}, which improves electronic charge carrier concentration. Promising n-type conductivity of trivalent ions doped $SrTiO_3$ is attained at the anode operating conditions. The electrochemical properties of perovskite metal oxides mainly depend on the B-O-B bond interaction, and any change in the electronic structure due to B-site doping modifies the electrochemical and electrical properties of the resulting material. Furthermore, B-site doping will significantly increase the thermodynamic stability in both oxidizing and reducing atmospheres. In $SrTiO_3$, acceptor doping such as Co^{3+}, Mn^{3+}, and Fe^{3+} on the B-site (Ti^{4+}) can increase the oxygen vacancy concentration.[13] The formed oxygen vacancies may provide active sites for fuel oxidation in anodes. Meanwhile, A and B site doping with Y^{3+} and Fe^{3+} in $SrTiO_3$ shows higher electrical conductivity and phase stability in air

and H_2 atmospheres.[14] Also, B-site doping by Fe can enhance the catalytic activity of the resulting material.[15]

In this paper we report the synthesis and fabrication of anodes by the infiltration of $Y_{0.08}Sr_{0.88}TiO_{3-\delta}$ (YST) and $Y_{0.08}Sr_{0.92}Ti_{1-x}Fe_xO_{3-\delta}$ (YSTF) into YSZ scaffolds. We study the effects of Fe doping in $Y_{0.08}Sr_{0.92}Ti_{1-x}Fe_xO_{3-\delta}$ ($x = 0, 0.2, 0.4$)-YSZ. In YST, A-site deficiency was introduced to suppress impurity (pyrochlore $Y_2Ti_2O_7$) phase formation. The stability, electrical conductivity, and microstructure of YST and YSTF were investigated. The electrochemical properties of the YST-YSZ and YSTF-YSZ composite anodes were studied between 973–1073 K.

Experimental

The electrolyte support cell used in this study was made by tape casting, with the outer two layers having pore formers as reported elsewhere.[11] An 85 µm dense YSZ electrolyte disk was sandwiched between two 50 µm porous YSZ layers. The diameter of the porous YSZ region was 0.67 cm.
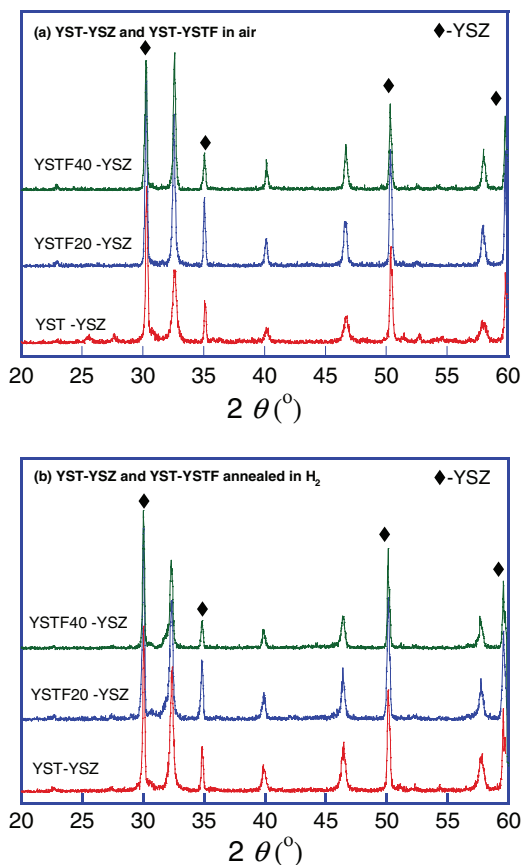
To prepare composites of YST-YSZ and YSTF-YSZ, we first prepared precursor solutions from $Y(NO_3)_3 \cdot 6H_2O$ (Acros Organics, 99.9%), $Sr(NO_3)_2$ (Sigma Aldrich, ACS 99%), $[CH_3CH(O)CO_2 \cdot NH_4]_2.Ti(OH)_2$ [dihydroxy-bis-ammonium lactate titanium (IV), Alfa Aesar], and $Fe(NO_3)_3 \cdot 9H_2O$ (Sigma Aldrich, ACS 98%) were dissolved in water at a molar ratio of 0.08:0.88:1 (YST), 0.08:0.92:0.2:0.8 (YSTF20), and 0.08:0.92:0.4:0.6 (YSTF40), respectively, along with citric acid. YST-YSZ and YSTF-YSZ anodes were prepared by infiltrating precursor solution into the anode side of the three-layered YSZ backbone. YST and YSTF were infiltrated into YSZ by a multi-step process followed by heating at 723 K to decompose nitrates and citric acid. Infiltration has been repeated until 40 wt% loading of oxide was achieved. Finally, the YST-YSZ and YSTF-YSZ wafers were calcined in air at 1273 K. The LSF ($La_{0.8}Sr_{0.2}FeO_3$)-YSZ cathode was fabricated by infiltration with an aqueous solution of $La(NO_3)_3 \cdot 6H_2O$, $Sr(NO_3)_2$, and $Fe(NO_3)_3 \cdot 9H_2O$ on porous YSZ opposite the anode layer, and then calcined in air at 1123 K. 1 wt% Pd and 10 wt% ceria were also infiltrated into the anode and 1 wt% Pd into the cathode as catalysts and heated in air at 723 K.

Electrical conductivity of YST-YSZ and YSTF-YSZ was measured as a function of temperature using the standard four-probe technique with a BioLogic Potentiostat. Samples for conductivity measurement were prepared by the infiltration of YST and YSTF into a porous YSZ slab (2.2 mm × 5.3 mm × 9.9 mm in size).

The initial structural characterization of the sintered product was performed by X-ray diffractometry using a Rigaku diffractometer (Cu Ka radiation, 40 kV, 30 mA) to confirm the structure with a scan rate of 0.5° min^{-1} and a diffraction range of $20° < 2\theta < 60°$.

*Electrochemical Society Active Member.
zE-mail: gtkim@unist.ac.kr

Figure 1. XRD patterns of YST-YSZ and YSTF-YSZ. (a) YST-YSZ and YSTF-YSZ sintered at 1273 K for 4 h in air. (b) YST-YSZ and YSTF-YSZ annealed in H_2 at 1073 K for 10 h.

Figure 2. A high-resolution SEM image of YST-YSZ and YSTF-YSZ. (a) YST, (b) YSTF20-YSZ, and (c) YSTF40-YSZ sintered at 1273 K for 4 h in air. (d) YST, (e) YSTF20-YSZ, and (f) YSTF40-YSZ after annealed in H_2 at 1073 K for 10 h.

The morphological features of the composites were examined with scanning electron microscopy. Ag paste and Ag wire were used for electrical connections in both the anode and cathode. The anode was exposed to humidified (3% H_2O) H_2 with a flow rate of 20 mL min^{-1} and the cathode was left open in air. Impedance spectra and *V–i* polarization curves were measured using a BioLogic Potentiostat.

Results and Discussion

In order to effectively function as the anode for a SOFC, the anode material should possess both chemical stability and structural stability under the anode operating conditions. Other factors such as microstructure, porosity, and physical binding between the electrode-electrolyte interfaces are also important for cell processing parameters to achieve good electrochemical performance. The above requirements can be easily achieved by laminating YSZ green tape and by infiltration of respective metal salts on the porous YSZ backbone.[16]

X-ray diffraction and SEM were performed on the electrolyte support cell in order to understand the structural stability and morphological changes of the YST-YSZ and YSTF-YSZ anodes. The XRD patterns of YST-YSZ and YSTF-YSZ are shown in Fig. 1. It can be seen that YST and YSTF perovskite phases were formed after sintering and there is no evidence of solid state reaction with YSZ. The stability of YST-YSZ and YSTF-YSZ under the anode operating conditions was further explored by annealing under a H_2 atmosphere at 1073 K for 10 h, as shown in Fig. 1b. The formed YST and YSTF phases show chemical stability with YSZ and the perovskite structure is successfully preserved under a reducing atmosphere. Fagg et. al. also reported that substitution of La^{3+} for the Sr^{2+} site increases the stability of SrTi$_{1-x}$Fe$_x$O$_{3-\delta}$ perovskite materials significantly in a H_2 atmosphere and inhibits solid state reaction with YSZ.[17]
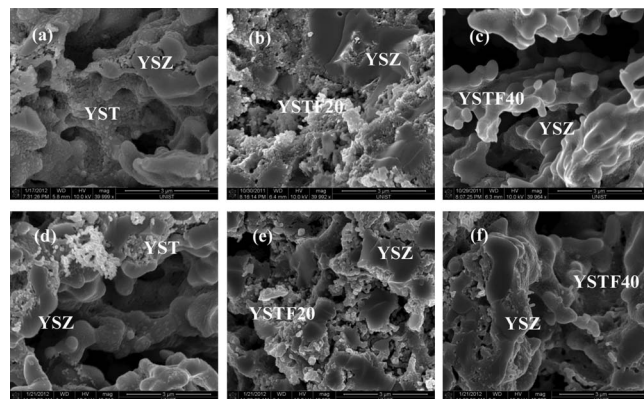
The cross-sectional microstructures of YST-YSZ and YSTF-YSZ anodes of the electrolyte support cell observed by SEM are shown in Fig. 2. The impregnated YST and YSTF formed as particles, which are easily distinguishable from the porous YSZ scaffold. In Fig. 2a the YST appear as well-connected small particles spread over the YSZ scaffolds. The addition of 20% Fe in YST (Fig. 2b YSTF20) forms more fine YSTF particles over the porous YSZ scaffolds. YSTF40 (Fig. 2c), however, forms a dense covered layer over the entire porous YSZ scaffolds, which could decrease the fuel cell performance due to the reduction of the number of triple phase boundaries (TPB).

In order to better understand the change in microstructure that occurred in the YST and YSTF layers under the fuel cell operating conditions, the YST-YSZ and YSTF-YSZ anodes were treated in humidified H_2 at 1073 K for 10 h. Figs. 2d, 2e, and 2f show micrographs of H_2 treated YST, YSTF20, and YSTF40, respectively. Upon treatment at 1073 K in H_2, the microstructure of YST and YSTF remains close to that of the sample treated only in air at 1273 K. There is no significant change in the microstructure of YST-YSZ and YSTF-YSZ.

To quantify the surface area in the YST and YSTF layers upon annealing at 1073 K in humidified H_2, BET isotherms were obtained on the samples and the results are summarized in Table I. The YSTF20-YSZ electrode shows higher surface area (1.189 m^2 g^{-1}) than the YST (0.577 m^2 g^{-1}) and YSTF 40 (0.701 m^2 g^{-1}). In YSTF20, under the anode operating conditions, a nanoporous conductive layer with larger surface area is formed on the porous YSZ scaffold. The higher surface area provides an extended TPB in the anode, which significantly improves the electrochemical performance.

The electrical conductivities of YST-YSZ and YSTF-YSZ sintered at 1273 K in air are shown in Fig. 3a as a function of temperature in air. The electrical conductivity measurements in air and H_2 were conducted during a cooling process from 1073 K to 673 K. It can be observed that the electrical conductivity for YST-YSZ and YSTF-YSZ, respectively, increases with increasing temperature. Fig. 3b shows the electrical conductivity measured in humidified H_2, revealing an increase compared with the results for YST-YSZ and YSTF-YSZ measured in air. The enhanced electrical conductivity in a reducing atmosphere can be explained as follows:

Table I. Specific surface area of YST-YSZ and YSTF-YSZ anodes annealed in H_2 at 1073 K for 10 h.

| Composition	Surface area (m^2 g^{-1})
YST-YSZ	0.577
YSTF20-YSZ	1.189
YSTF40-YSZ	0.701
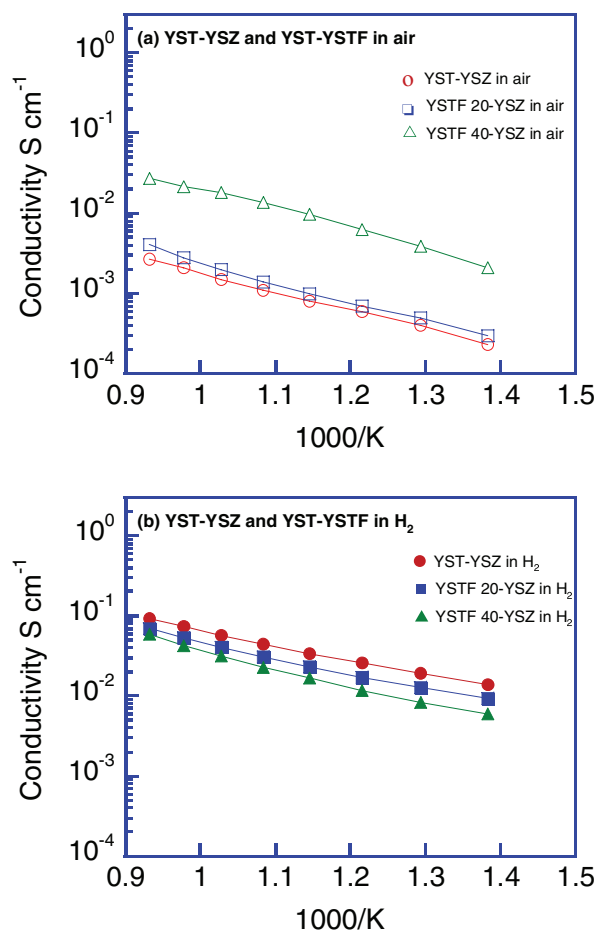
Figure 3. (a) The Arrhenius plot of electrical conductivity measured in air for YST-YSZ and YSTF-YSZ sintered in air at 1273 K. (b) The Arrhenius plot of electrical conductivity measured in H_2 for YST-YSZ and YSTF-YSZ.

Under a reducing condition, in a donor doped (Y^{+3}) system electrons are generated by the creation of oxygen vacancies from the YST lattice according to the following reaction.

$$2Ti_{Ti}^{\times} + O_O^{\times} \rightarrow 2Ti_{Ti}' + V_O^{\bullet\bullet} + \frac{1}{2}O_2$$
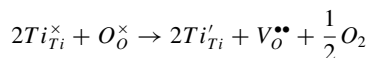
The extra electrons generated at Ti sites may enter into the conduction band, and conductivity increases upon reduction.[18] Similarly, acceptor (Fe^{3+}) doping in $SrTiO_3$ results in the formation of positive charged holes in the valence band.

$$Fe_{Ti}^{\times} \leftrightarrows Fe_{Ti}' + h^{\bullet}$$
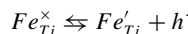
The positively charged holes formed in the valence band provide electron conduction paths.

In YSTF-YSZ, a donor (Y^{3+}) and acceptor (Fe^{3+}) co-doped system, the electrical conductivity decreases with increasing Fe content under a reducing condition, which suggests a decreased concentration of Ti^{3+} in YSTF-YSZ.[19] In the YSTF co-doped system the electrical conductivity is the result of electronic defects generated by acceptors and donors.[12] Therefore, extra electrons generated by the donor (Y^{3+}) may be neutralized by the holes created by the acceptor (Fe^{3+}).

$$null \leftrightarrows e' + h^{\bullet}$$
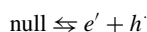
The electrical conductivity thus decreases with increasing Fe doping concentration in donor (Y^{3+}) and acceptor (Fe^{3+}) co-doped $SrTiO_3$ (Fig. 3b).

Figure 4 shows the *V-i* and power density curves for YST-YSZ and YSTF-YSZ anodes at 973–1023 K. An oxidation catalyst (1 wt% Pd supported on 10 wt% CeO_2) is added in order to achieve high
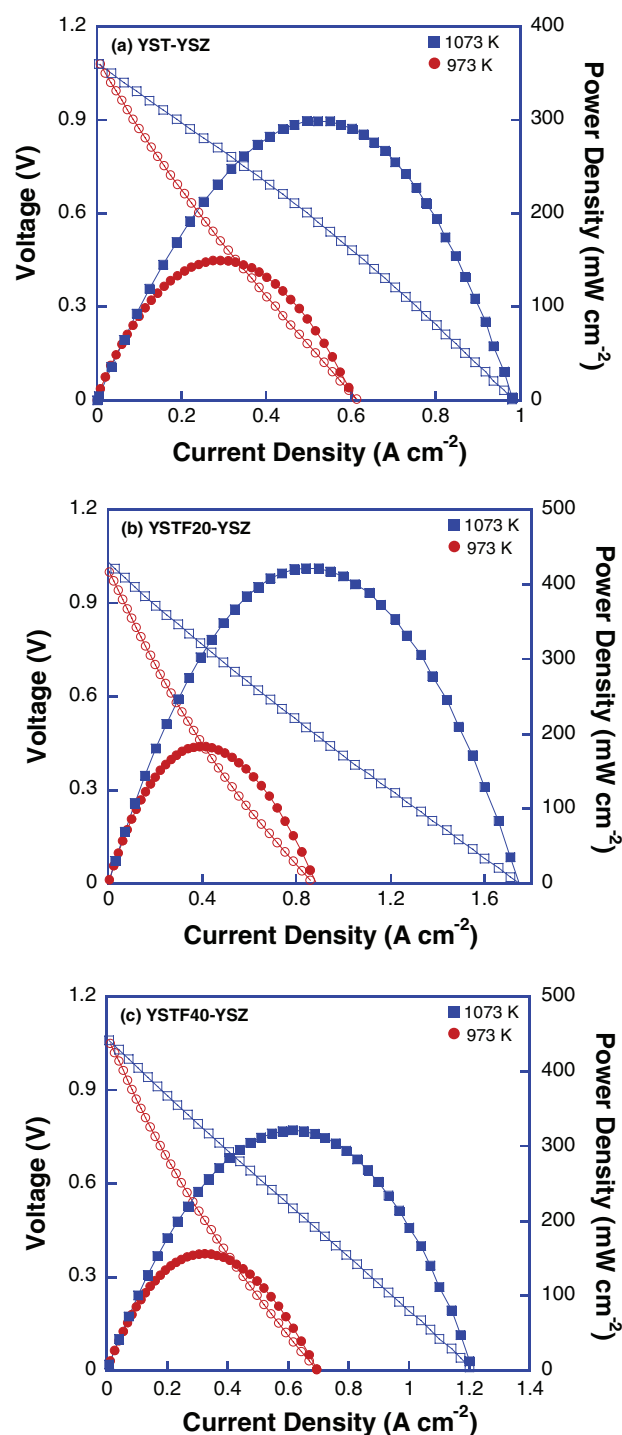
Figure 4. *V-i* polarization curves for the cells having an anode prepared by infiltration with Pd/CeO_2 catalyst. The data were obtained in H_2. (a) YST-YSZ, (b) YSTF20-YSZ and (c) YSTF40-YSZ. (Closed symbols designates *V* and open symbols designates power density).

performance.[11,20] All the cells show a reasonable open circuit potential (OCV) close to the theoretical Nernst potential, ~1.1 V at 973 K, suggesting that the cell was tightly sealed and the YSZ electrolyte was dense without pinholes or micro-cracks. The YST-YSZ, YSTF20-YSZ, and YSTF40-YSZ cells delivered power densities of 298, 421, and 321 mW cm^{-2}, respectively, at 1073 K. The power density of the YSTF20-YSZ shows 41% and 31% superior performance by compared to those of YST-YSZ and YSTF40-YSZ, respectively, at 1073 K. The power densities of the YST-YSZ and YSTF-YSZ anodes

Table II. The summary of electrochemical performance for YST-YST and YSTF-YST cells in H$_2$ with Pd/CeO$_2$ catalyst.

		YSTF + YSZ	
Temperature	YST + YSZ	Fe 20%	Fe 40%
973 K	149	183	156
1073 K	298	421	321
1273 K*	350		
1073 K*	71		

The power densities are given in mW cm^{-2}.
*Power density of YST-YSZ prepared by screen printing technique.[15,16,23]

at 973 K and 1073 K in H$_2$ are summarized in Table II. YST-YSZ and YSTF-YSZ prepared by infiltration show improved performance compared to that obtained with conventional screen printing.[15,16] In a reported YST-YSZ cell, YST is a bulk material fabricated by a screen printing technique and the cell delivers a power density of 350 mW cm^{-2} at 1273 K. In the present work, the fuel cell with 20% Fe doped YST infiltrated on a porous YSZ scaffold shows higher cell performance of 421 mW cm^{-2} even at a low operating temperature of 1073K.[15,16] It should also be noted that Ni metals (10 wt%) were previously introduced to YST-YSZ composite anodes in an effort to enhance the electrochemical performance.[15,16] However, in this study, even with cerium oxide (10 wt%) and Pd (1 wt%) as a catalyst instead of Ni, superior performance could be achieved while avoiding the vulnerability of Ni catalyst to sulfur contaminants.

Figure 5 shows the corresponding impedance plots of YST-YSZ and YSTF-YSZ anodes measured in H$_2$ at 973–1073 K under OCV condition. The ohmic and non-ohmic resistances are summarized in Table III. The ohmic losses of YST, YSTF20, and YSTF40 are 0.34, 0.33, and 0.35 Ω cm^2, respectively, at 1073 K. The ohmic resistances are higher than the losses expected for 85 μm YSZ electrolyte, 0.20 Ω cm^2. This may originate from the low electrical conductivity of YST-YSZ and YSTF-YSZ.[21]

In the YSTF20-YSZ anode, the Fe dopant helps to form particles that are distinct from the YSZ scaffolds. The particles of YST were broken up into nanoscale particles by 20% Fe doping in YST, which covers the porous YSZ surface. Under fuel cell operating conditions, the formed nanoscale YSTF20 particles ensure a high TPB length for electrochemical reactions in the anode. However, the Fe doped YSTF40-YSZ composite forms a dense coating layer on the YSZ scaffolds, which may limit the TPB length and subsequently increase the polarization loss in the anode. It seems that there is a different behavior of a YSTF20 and YSTF40 on a solid surface in wetting YSZ surface or forming a particle on YSZ surface.[22] In this context, the better performance of the YSTF20-YSZ anode is attributed to the significantly improved TPB.

Among the investigated YST-YSZ and YSTF-YSZ anodes, YSTF20-YSZ displays the best performance with the lowest anode polarization resistance, primarily due to the extended TPB at 1073 K.
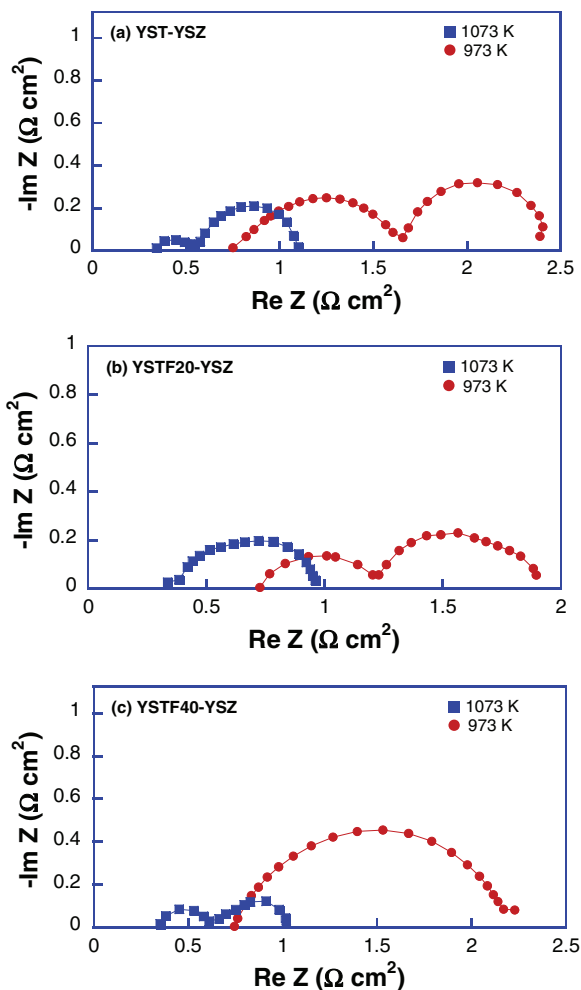
Figure 5. Impedance curves for the cells having an anode prepared by infiltration with Pd/CeO$_2$ catalyst. The data were obtained in H$_2$. (a) YST-YSZ, (b) YSTF20-YSZ and (c) YSTF40-YSZ.

Conclusions

The electrochemical properties of YST-YSZ and YSTF-YSZ composite anodes formed by infiltration on porous YSZ scaffolds were investigated. The XRD pattern shows YST and YSTF are stable with YSZ in both the as prepared state and anode operating conditions. Fe doping in YST plays an important role in optimizing the anode microstructure. The electrical conductivity of YST infiltrated YSZ and YSTF infiltrated YSZ anodes shows semiconducting behavior in both air and H$_2$ atmospheres. The electrical conductivity of YST-YSZ strongly depends on the Fe doping concentration. An electrolyte support cell with 40 wt% YSTF20 as an anode along with a Pd/CeO$_2$ catalyst and LSF as cathode shows a peak power density of 421 mW cm^{-2} at 1073 K. YST and YSTF40 show peak power density of

Table III. The summary of ohmic and non-ohmic resistance for YST-YSZ and YSTF-YSZ cells in H$_2$ with Pd/CeO$_2$ catalyst.

	YST + YSZ		YSTF + YSZ			
			Fe 20%		Fe 40%	
Temperature	ohmic	non-ohmic	ohmic	non-ohmic	ohmic	non-ohmic
973 K	0.75	1.7	0.72	1.17	0.74	1.48
1023 K	0.34	0.76	0.33	0.73	0.35	0.66

The ohmic and non-ohmic resistance is given in Ω cm^2.

298 and 321 mW cm^{-2}, respectively, at 1073 K. The infiltration technique shows better performance compared to conventional fabrication processes such as the screen printing method. The excellent performance of the YSTF20-YSZ anode is attributed to an increased TPB of YSTF20-YSZ compared to YST-YSZ and YSTF40-YSZ. The results show that YSTF20-YSZ with an added catalyst is a promising anode for IT-SOFC applications.

References

1. E. Baur and H. Preis, *Zeitschrift für Elektrochemie und angewandte physikalische Chiemiei*, **43**, 727 (1937).
2. E. P. Murray, T. Tsai, and S. A. Barnett, *Nature*, **400**, 649 (1999).
3. S. Park, J. M. Vohs, and R. J. Gorte, *Nature*, **404**, 265 (2000).
4. T. Hibino, A. Hashimoto, T. Inoue, J.-i. Tokuno, S.-i. Yoshida, and M. Sano, *Science*, **288**, 2031 (2000).
5. Y.-H. Huang, R. I. Dass, Z.-L. Xing, and J. B. Goodenough, *Science*, **312**, 254 (2006).
6. S. Yoo, T.-H. Lim, J. Shin, and G. Kim, *J. Power Sources*, **226**, 1 (2013).
7. S. Choi, J. Shin, K. M. Ok, and G. Kim, *Electrochim. Acta*, **81**, 217 (2012).
8. A. Atkinson, S. Barnett, R. J. Gorte, J. T. S. Irvine, A. J. McEvoy, M. Mogensen, S. C. Singhal, and J. Vohs, *Nat. Mater*, **3**, 17 (2004).
9. L. Yang, S. Wang, K. Blinn, M. Liu, Z. Liu, Z. Cheng, and M. Liu, *Science*, **326**, 126 (2009).
10. S. Tao and J. T. S. Irvine, *Nat. Mater*, **2**, 320 (2003).
11. S. Sengodan, H. J. Yeo, J. Y. Shin, and G. Kim, *J. Power Sources*, **196**, 3083 (2011).
12. S. Hui and A. Petric, *J. Electrochem. Soc.*, **149**, J1 (2002).
13. K. T. Lee and A. Manthiram, *Solid State Ionics*, **178**, 995 (2007).
14. J. S. Yoon, M. Y. Yoon, C. Kwak, H. J. Park, S. M. Lee, K. H. Lee, and H. J. Hwang, *Materials Science and Engineering: B*, **177**, 151 (2012).
15. J. Yoon, Y. Kim, E. Lee, M. Ji, B. Choi, and H. Hwang, *Electron. Mater. Lett.*, **7**, 209 (2011).
16. S. Choi, S. Yoo, J.-Y. Shin, and G. Kim, *J. Electrochem. Soc.*, **158**, B995 (2011).
17. D. P. Fagg, V. V. Kharton, J. R. Frade, and A. A. L. Ferreira, *Solid State Ionics*, **156**, 45 (2003).
18. Q. X. Fu, S. B. Mi, E. Wessel, and F. Tietz, *J. Eur. Ceram. Soc.*, **28**, 811 (2008).
19. S. Hui and A. Petric, *Mater. Res. Bull.*, **37**, 1215 (2002).
20. G. Kim, G. Corre, J. T. S. Irvine, J. M. Vohs, and R. J. Gorte, *Electrochem. Solid-State Lett.*, **11**, B16 (2008).
21. H. He, Y. Huang, J. M. Vohs, and R. J. Gorte, *Solid State Ionics*, **175**, 171 (2004).
22. G. Corre, G. Kim, M. Cassidy, J. M. Vohs, R. J. Gorte, and J. T. S. Irvine, *Chem. Mater.*, **21**, 1077 (2009).
23. X. Sun, S. Wang, Z. Wang, J. Qian, T. Wen, and F. Huang, *J. Power Sources*, **187**, 85 (2009).